Temperature-insensitive refractive index sensor based on Mach–Zehnder interferometer with two microcavities

Yinfeng Wang (汪银风)[1], Sumei Wang (王素梅)[1,*], Lan Jiang (姜 澜)[1], Hua Huang (黄 华)[2], Liuchao Zhang (张柳超)[3], Peng Wang (王 鹏)[1], Lingya Lv (吕灵亚)[1], and Zhitao Cao (曹志涛)[1]

[1]*Laser Micro/Nano Fabrication Laboratory, School of Mechanical Engineering, Beijing Institute of Technology, Beijing 100081, China*

[2]*Vibration and Noise Control Laboratory, School of Mechanical Engineering, Beijing Institute of Technology, Beijing 100081, China*

[3]*School of Optoelectronics, Beijing Institute of Technology, Beijing 100081, China*

**Corresponding author: wangsumei@bit.edu.cn*

Received October 19, 2016; accepted December 6, 2016; posted online January 16, 2017

We propose a temperature-insensitive refractive index (RI) fiber sensor based on a Mach–Zehnder interferometer. The sensor with high sensitivity and a robust structure is fabricated by splicing a short photonic crystal fiber (PCF) between two single-mode fibers, where two microcavities are formed at both junctions because of the collapse of the PCF air holes. The microcavity with a larger equatorial dimension can excite higher-order cladding modes, so the sensor presents a high RI sensitivity, which can reach 244.16 nm/RIU in the RI range of 1.333–1.3778. Meanwhile it has a low temperature sensitivity of 0.005 nm/°C in the range of 33°C–360°C.

OCIS codes: 060.2280, 060.2370.
doi: 10.3788/COL201715.020603.

Optical fiber sensors are widely used in physical parameter detection, such as refractive index (RI), temperature, pressure, strain, humidity, and bending sensing[1–7], due to their characteristics of high sensitivity, immunity to electromagnetism, resistance to chemical corrosion, compact size, fast response, etc. Coelho *et al.* proposed a long period grating coated with titanium dioxide thin films[8], where a wavelength sensitivity of 825 nm/RIU was achieved in the range 1.46 to 1.48, but the procedure of coating thin films is complicated. Pevec *et al.* fabricated a silica nanowire-based RI sensor[9], and a sensitivity in excess of 800 nm/RIU was demonstrated within an aquatic medium. Gao proposed a microfiber-enabled Fabry–Perot interferometer constructed by splicing a section of microfiber between two cleaved standard single-mode fibers (SMFs)[10], where a high RI sensitivity of 1330.8 nm/RIU was achieved. Recently, several types of in-line fiber Mach–Zehnder mode interferometers for RI sensing have been reported. Yang *et al.* proposed a microcavities-based fiber sensor by concatenating two micro air cavities fabricated by combining the techniques of femtosecond laser micromachining and arc fusion splicing[11], where a wavelength sensitivity of 172.4 nm/RIU was achieved in the RI range of 1.333–1.365, but the fabrication with the femtosecond laser is time-consuming and expensive. The progress in photonic crystal fiber (PCF) sensors opens a new possibility for the measurements of the RI[12–15]. Wang *et al.* presented a splicing points tapered SMF-PCF-SMF Mach–Zehnder interferometer (MZI)[12]. This kind of sensor with a tapered waist diameter of 60.4 μm realized the RI sensitivity of 260.8 nm/RIU, however, the decrease of the fiber diameter makes it too fragile to be applied widely. Ni *et al.* fabricated a hybrid structured in-line MZI for the simultaneous measurement of the RI and temperature. The MZI is composed of an embedded slender air cavity in a micro fiber cascaded to a piece of PCF[13], where the RI sensitivity and temperature are 55.84 nm/RIU and 0.143 nm/°C. This kind of sensor measured the RI and temperature simultaneously, which is complex, and it has a low RI sensitivity. Zhao *et al.* proposed a sensitivity-enhanced PCF RI sensor with two waist-broadened tapers and one waist-thinned taper[14], where a maximum RI linear sensitivity of 281.6 nm/RIU was obtained, but the existence of three tapers greatly increased the transmission loss.

In this study, we proposed an easily fabricated and robust RI sensor with high sensitivity, which consists of a section of a PCF and two microcavities. The micrcavities embedded in the optical fiber were fabricated by splicing a piece of the PCF between two sections of SMFs. Higher-order cladding modes can be excited by the first microcavity with a large equatorial dimension, and coupled from the SMF core to the PCF cladding by the second microcavity. The experiment results show that the sensitivity of the sensor can reach 244.16 nm/RIU in the RI range of 1.333–1.3778, and the RI response has good linearity and high repeatability.

The proposed MZI for the RI measurement was fabricated by using the fusion technique. The schematic diagram of the sensor is shown in Fig. 1. The sensor head consists of a section of a PCF and two microcavities. The two microcavities were fabricated by using the manual mode of a commercial fusion splicer (Model IFS-9, INNO INSTRUMENT, Inc., Korea).

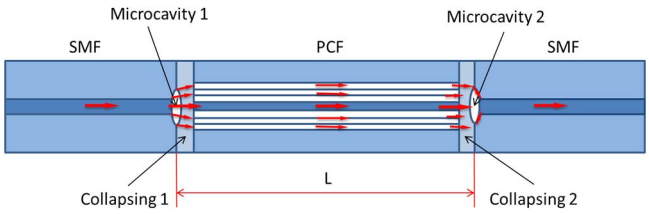

Fig. 1. Schematic diagram of the microcavities-based MZI.

In the fabrication, different discharging locations and splicing parameters can result in different splicing phenomena. When discharging at the side of the SMF about 30 μm away from the junction, no microcavity was formed. However, when discharging at the side of the PCF about 30 μm away from the junction, a microcavity was formed. Because of the high arc discharge, the PCF air holes around the splicing point collapsed entirely, and the air in the air holes was pressed to the splicing point, thus, a microcavity was fabricated at the junction of the SMF and PCF. The microscopic image of the PCF cross-section is shown in Fig. 2(a). This PCF consists of a solid core surrounded by five rings of air holes arranged in a hexagonal pattern. The core diameter is ~7 μm, the average diameter of the air holes is ~3.3 μm, and the average pitch (hole-to-hole distance) is ~6.1 μm. The PCF was cut off 15 mm away from the junction, then, another SMF was spliced with the PCF. Through the method mentioned above, we fabricated the microcavities-based MZI.

In this Letter, we fabricated one direct splicing MZI (sensor 1) and three microcavities-based MZIs with different microcavity sizes to demonstrate their RI sensing properties. We fabricated these three sensors with almost the same discharge location, the same arc time of 500 ms, and the same interference length of 15 mm. Different arc power was used to form different microcavity sizes. The microcavity sizes and related arc power are shown in Table 1. The microscopic images of microcavity 1 of sensors 2, 3, and 4 are shown in Figs. 2(b)–2(d), and the collapsed area is shown in Fig. 2(e).

When the arc power increases, the size of the microcavity will become larger, and the shape of the microcavity will become rounder, namely, the curvature of ellipse at the longitudinal direction will increase. Because we studied the RI sensing property of the sensor, we first measured the spectra of the sensors in distilled water. The interference spectra of sensors 1, 2, 3, and 4 in distilled water are shown in Fig. 3. It can be seen that the spectrum insertion loss of sensor 4 is larger than that of sensor 1, which is because the two extra microcavities and the longer collapse areas of sensor 4 will increase the loss of light transmission. Also, along with the arc power increasing, the length of the collapsed area will increase, and the insertion loss of the spectrum will increase too.

As displayed in Fig. 1, when light emitted from a tunable laser transmits from the SMF into microcavity 1, part of the light in the SMF core will be dispersed by microcavity 1 and coupled into higher-order cladding modes. Another part of the light will pass through microcavity

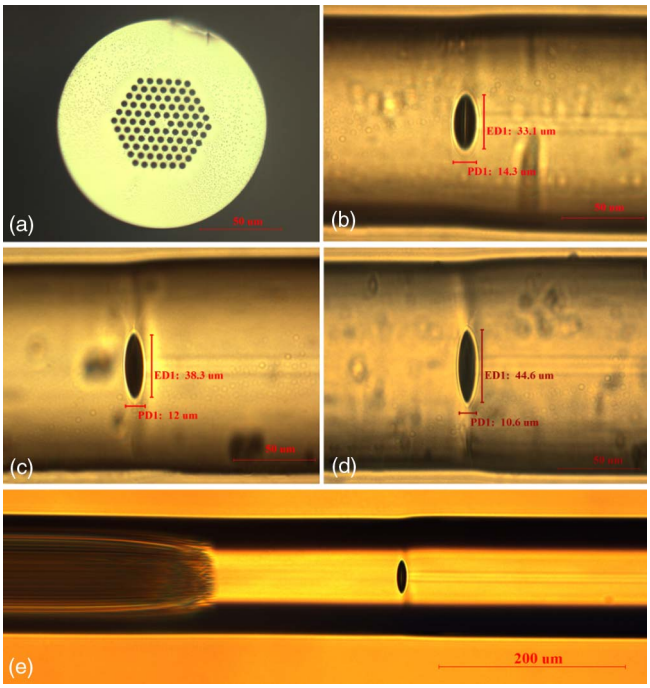

Fig. 2. Microscopic image of (a) the PCF cross-section, (b) microcavity 1 of sensor 2, (c) microcavity 1 of sensor 3, (d) microcavity 1 of sensor 4, and (e) microcavity and collapse area.

Table 1. Microcavity Sizes and Related Arc Power[a]

Parameters	Sensor 2	Sensor 3	Sensor 4
Arc power (%)	70%	60%	50%
ED 1 (μm)	33.1	38.3	44.6
PD 1 (μm)	14.3	12.0	10.6
ED 2 (μm)	30.9	36.6	42.9
PD 2 (μm)	15.1	13.1	10.0

[a]ED is the equatorial diameter of the microcavity, PD is the polar diameter of the microcavity. ED 1 and PD 1 are the sizes of microcavity 1, and ED 2 and PD 2 are the sizes of microcavity 2.

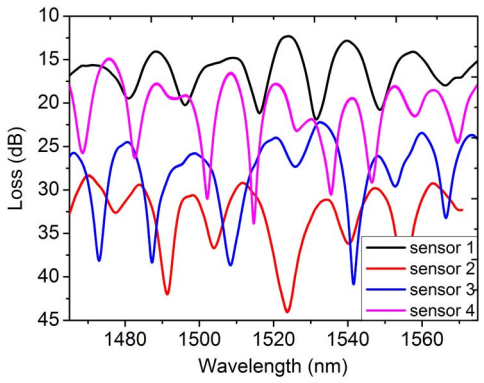

Fig. 3. Transmission spectra of the sensors 1, 2, 3, and 4.

1 and continue to propagate forward in the PCF core. Parts of the light transmitting in the PCF cladding will be coupled back to the SMF core when they transmit through microcavity 2, and then interferences will occur.

Due to the different effective RI of the PCF core and cladding, there will be an optical path difference in the same transmission distance between two light beams. In general, the interference pattern intensity is the function of the intensities of the fundamental mode and the cladding mode, it can be the simplified as

$$I = I_1 + I_2 + 2\sqrt{I_1 I_2}\cos\varphi, \tag{1}$$

where I_1 and I_2 are the light intensities transmitting in the core and cladding, respectively. φ is the phase difference, and it is shown as

$$\varphi = \frac{2\pi\Delta n_{\text{eff}} L}{\lambda} = \frac{2\pi(n_{\text{eff}}^{\text{core}} - n_{\text{eff}}^{\text{cladding}})L}{\lambda}, \tag{2}$$

where L is the optical route length of the interferometer, namely, it is the distance between the two microcavities, and λ is the light wavelength. Δn_{eff} is the effective RI's difference between the core and cladding mode, it can be given as

$$\Delta n_{\text{eff}} = n_{\text{eff}}^{\text{core}} - n_{\text{eff}}^{\text{cladding}}, \tag{3}$$

where $n_{\text{eff}}^{\text{core}}$, $n_{\text{eff}}^{\text{cladding}}$ are the effective RIs of the core mode and the cladding mode, respectively. Transmission dips appear when phase difference φ is satisfied with the equation of $\varphi = 2m + 1$, where m is a positive integer. Thus, if light emitted from a broadband optical source is launched into the MZI, the transmission spectrum would exhibit a series of periodical sinusoidal oscillations. The m-order resonance wavelength can be given as

$$\lambda_m = \frac{2(n_{\text{eff}}^{\text{core}} - n_{\text{eff}}^{\text{cladding}})L}{2m+1} = \frac{2\Delta n_{\text{eff}} L}{2m+1}. \tag{4}$$

The free spectral range (FSR) of the fabricated MZI can be expressed as

$$\text{FSR} = \lambda_{m-1} - \lambda_m = \frac{4\Delta n_{\text{eff}} L}{(2m-1)(2m+1)} = \frac{\lambda_m \lambda_{m-1}}{\Delta n_{\text{eff}} L}. \tag{5}$$

When the surrounding RI changes, the evanescent field in the MZI will change, and $n_{\text{eff}}^{\text{cladding}}$ and Δn_{eff} will change as well. Then, the wavelength of the m-order interference valley will change. The wavelength shift is shown as

$$\Delta\lambda_m = \frac{2(\Delta n + \Delta n_{\text{eff}})L}{2m+1} - \frac{2\Delta n_{\text{eff}} L}{2m+1} = \frac{2\Delta n L}{2m+1}, \tag{6}$$

where Δn is the variation of the effective RI of the PCF cladding along with the changing of the external RI.

The RI measurements of the proposed MZIs were carried out in a clean room with an almost constant temperature and humidity in order to eliminate the effects caused by temperature and humidity fluctuations. A detection system was employed to monitor the transmission spectra of the MZIs. The detection system consists of a tunable laser (Agilent 81980A, Agilent Technologies Inc.) and an optical power meter (81636B, Agilent Technologies Inc.). The sensors were connected to the detection system by two SMF jumpers. The tunable laser scans through its wavelength range (1465–1575 nm) at the rate of 5 pm per step. During the measurements, the sensors were straightened and fixed on fiber holders to avoid a bending-induced and force-induced signal change, and the fiber holders were supported by a three-dimensional microtranslation stage to adjust the height of the sensor. The test solution was dropped on a glass slide right under the fiber sensor. The NaCl solutions of different mass percent concentrations (0%, 5%, 10%, 15%, 20%, and 25%) were used in the experiments. The corresponding RIs are 1.3330, 1.3418, 1.3505, 1.3594, 1.3684, and 1.3778, respectively.

In every measurement, we injected the RI solution and made sure the sensing head was totally immersed in the solution, and then measured and saved the spectrum. After each measurement, the NaCl solution was removed. The glass and the fiber sensor head were cleaned with distilled water and alcohol, and then dried with a hairdryer until the spectrum was same as the reference spectrum in the air. Through the above operations, the RI sensing was experimentally demonstrated. From Figs. 4(a)–4(d), it can be seen that as the external RI increases, all of the transmission spectra shifted toward the longer wavelength.

In order to demonstrate the sensitivities of the microcavities-based MZIs, wavelength shifts of the corresponding transmission spectra with an external RI change are given, as shown in Fig. 5. The slopes of the linear fitting curves represent the RI sensitivities. The coefficients of determination R^2 are all above 0.98, indicating good linear properties. It can be seen that the RI measuring sensitivity of sensor 4 is much higher than that of sensor 1. Also, the

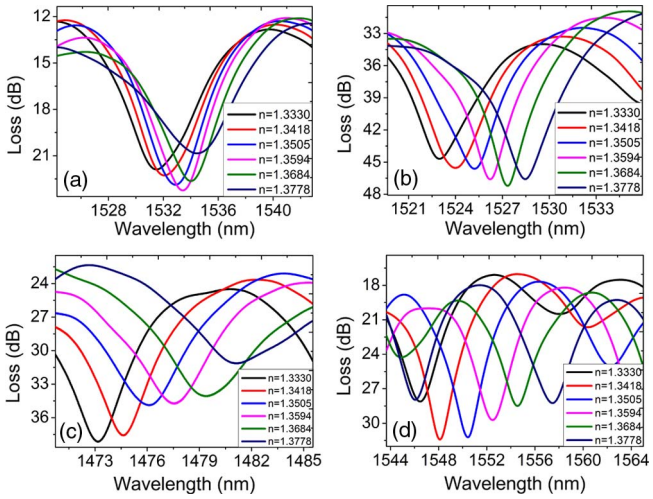

Fig. 4. Wavelength shifts of interference spectrum of (a) sensor 1, (b) sensor 2, (c) sensor 3, and (d) sensor 4.

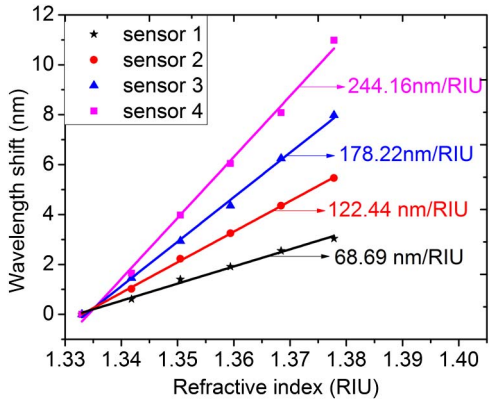

Fig. 5. Relations between wavelength shifts and the surrounding RI of different sensors.

RI sensitivity is higher for a sensor with a larger microcavity equatorial diameter. The sensitivity of the RI measurement can reach 244.16 nm/RIU with a mirocavity equatorial diameter of 44.6 μm, which is increased by 3.55 times that of the sensor without a microcavity, whose sensitivity is 68.69 nm/RIU.

The interference spectra of sensor 1 and sensor 4 are fast Fourier transformed to obtain the spatial frequency spectra, as is shown in Fig. 6, and, then, to determine and compare the number and the power distribution of the coupling modes. Obviously, the power is mostly distributed in the fundamental mode, and it is also distributed in the first several main cladding modes, while the other cladding modes have a very small contribution to the interference spectrum. It can be seen from Fig. 6 that the spatial frequency spectrum of the sensor 1 has only two main modes, the fundamental mode and one main cladding mode. However, at least three main cladding modes, including a higher order one, are observed in the spatial frequency spectrum of sensor 4. The reason is that the equatorial diameter of microcavity 1 of sensor 4 is much larger than that of the fiber core, and the elongated microcavity will excite higher-order cladding modes. When light passes through the SMF into microcavity 1, part of the light in the SMF core will be coupled into higher-order cladding modes. According to the RI definition, when the RI of the surrounding solution is smaller than that of the fiber cladding, the effective RI of the cladding will be reduced, while the effective RI of the fiber core remains the same. According to Eq. (3), when surrounding refractive is constant, the higher cladding modes excited by microcavity 1 will result in Δn_{eff} increasing. According to Eq. (4), the wavelength shift will increase, and the RI sensitivity will be improved. In conclusion, the existence of microcavities can improve the RI sensitivity of the sensor, where the larger the equatorial diameter of microcavity 1 is and the higher the order of cladding modes are excited, the more sensitive the sensor is.

The temperature property of sensor 4 was also investigated in a temperature range of 33°C–360°C by placing it in a tube furnace. The sensor was first heated to 400°C at the rate of 10°C/min and maintained for 1 h to eliminate the effect of mechanical stress caused by the fusion splicing process, and then cooled down to room temperature. For the second heating process, the temperature was increased from 33°C to 360°C at the rate of 5°C/min. We set the temperature of the tube furnace and calibrated the actual temperature in the tube with a standard thermocouple, then, we recorded the actual temperature and measured the spectrum at each temperature value. The linear fit of the wavelength shifts with the increase of temperature is shown in Fig. 7. It can be seen that the temperature sensitivity of sensor 4 is only 0.005 nm/°C. Thus, the corresponding RI measurement error due to the temperature effect is about 2.048×10^{-5} RIU/°C, which can be ignored.

We propose an MZI based on two microcavities for RI sensing. The sensor is fabricated by splicing a short of a PCF between two sections of SMFs. By discharging at both sides of the PCF, two microcavities are created at two junctions because of the total collapse of the PCF air holes. The high-order cladding modes are more sensitive to the surrounding RI changes, so the RI sensitivity of the sensor with larger microcavities is higher. In the RI range of 1.3330–1.3778, the RI sensitivity can reach 244.16 nm/RIU. The temperature experiment results show that the proposed sensor has low temperature sensitivity. Furthermore, because of no reduction in the fiber diameter direction,

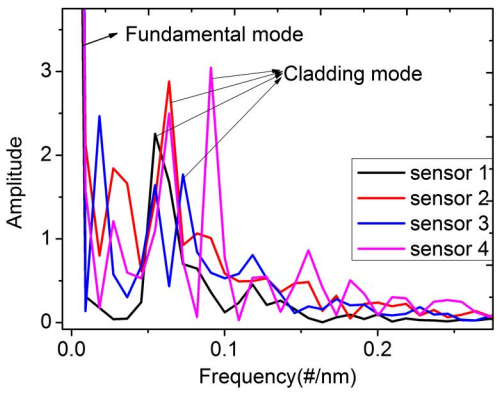

Fig. 6. Spatial frequency spectra of sensors 1 and 4.

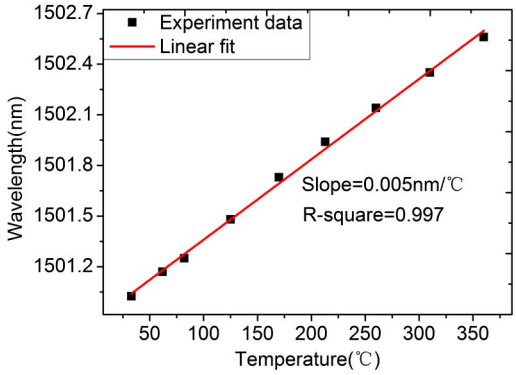

Fig. 7. Wavelength shifts with the increase of the temperatures for sensor 4.

the proposed structure is more robust than taper-based and trench structure fiber sensors.

This work was supported by the Ministry of Science and Technology of China (MOST) (No. 2015AA043504) and the National Natural Science Foundation of China (NSFC) (Nos. 91323301 and 51575053).

References

1. T. Liu, J. Yin, J. Jiang, K. Liu, S. Wang, and S. Zou, Opt. Lett. **40**, 1049 (2015).
2. B. Xu, C. Wang, D. N. Wang, Y. Liu, and Y. Li, Opt. Express **23**, 23484 (2015).
3. S. Liu, K. Yang, Y. Wang, J. Qu, C. Liao, J. He, Z. Li, G. Yin, B. Sun, J. Zhou, G. Wang, J. Tang, and J. Zhao, Sci. Rep. **5**, 7624 (2015).
4. J. Mathew, Y. Semenova, and G. Farrell, IEEE Sens. J. **13**, 1632 (2013).
5. D. Wu, Y. Zhao, and J. Li, Sens. Actuators B: Chem. **213**, 1 (2015).
6. P. Liu, L. Jiang, S. Wang, Z. Cao, and P. Wang, Chin. Opt. Lett. **14**, 020602 (2016).
7. Z. Yang, H. Sun, T. Gang, N. Liu, J. Li, F. Meng, X. Qiao, and M. Hu, Chin. Opt. Lett. **14**, 050604 (2016).
8. L. Coelho, D. Viegas, J. L. Santos, and J. M. M. M. de Almeida, Sens. Actuators B: Chem. **202**, 929 (2014).
9. S. Pevec and D. Donlagic, Appl. Phys. Lett. **102**, 213114 (2013).
10. S. C. Gao, W. G. Zhang, Z. Y. Bai, H. Zhang, W. Lin, L. Wang, and J. L. Li, J. Lightwave Technol. **32**, 1682 (2014).
11. Y. Jinpeng, J. Lan, W. Sumei, C. Qianghua, L. Benye, and X. Hai, IEEE Photon. J. **3**, 1189 (2011).
12. Q. Wang, L. Kong, Y. Dang, F. Xia, Y. Zhang, Y. Zhao, H. Hu, and J. Li, Sens. Actuators B: Chem. **225**, 213 (2016).
13. X. Ni, M. Wang, D. Guo, H. Hao, and J. Zhu, IEEE Photon. Technol. Lett. **28**, 1850 (2016).
14. Y. Zhao, F. Xia, and J. Li, J. Lightwave Technol. **34**, 1373 (2016).
15. Q. Liu and Q. Wang, Chin. Opt. Lett. **10**, 090601 (2012).